NANO · MICRO small
www.small-journal.com

Pseudocapacitance-Induced Synaptic Plasticity of Tribo-Phototronic Effect Between Ionic Liquid and 2D MoS_2

*Ribwar Ahmadi, Amin Abnavi, Amirhossein Hasani, Hamidreza Ghanbari, Mohammad Reza Mohammadzadeh, Mirette Fawzy, Fahmid Kabir, and Michael M. Adachi**

Contact-induced electrification, commonly referred to as triboelectrification, is the subject of extensive investigation at liquid–solid interfaces due to its wide range of applications in electrochemistry, energy harvesting, and sensors. This study examines the triboelectric between an ionic liquid and 2D MoS_2 under light illumination. Notably, when a liquid droplet slides across the MoS_2 surface, an increase in the generated current and voltage is observed in the forward direction, while a decrease is observed in the reverse direction. This suggests a memory-like tribo-phototronic effect between ionic liquid and 2D MoS_2. The underlying mechanism behind this tribo-phototronic synaptic plasticity is proposed to be ion adsorption/desorption processes resulting from pseudocapacitive deionization/ionization at the liquid–MoS_2 interface. This explanation is supported by the equivalent electrical circuit modeling, contact angle measurements, and electronic band diagrams. Furthermore, the influence of various factors such as velocity, step size, light wavelength and intensity, ion concentration, and bias voltage is thoroughly investigated. The artificial synaptic plasticity arising from this phenomenon exhibits significant synaptic features, including potentiation/inhibition, paired-pulse facilitation/depression, and short-term memory (STM) to long-term memory (LTM) transition. This research opens up promising avenues for the development of synaptic memory systems and intelligent sensing applications based on liquid–solid interfaces.

1. Introduction

Liquid–solid contact electrification (i.e., triboelectrification) is of great significance in electrochemistry due to its broad impact on water splitting, electrowetting, liquid–solid triboelectric nanogenerator (TENG) for harvesting blue energy, the direct current generation, and recently, tribovoltaics.[1–12] Tribovoltaics and photovoltaics are similar effects observed in semiconductors with the only difference in their energy quantum that are bindingtons and photons, respectively.[7,13] Bindingtons are generated upon sliding one material over another and can excite electron–hole pairs in the semiconductor. The excited electron–hole pairs are separated through the built-in electric field between the liquid and semiconductor, similar to the photovoltaic effect at the solid-state *p–n* junction. The actual identity of the charge carriers at the liquid–solid interface was unclear until Wang et. al through nano and macro scale measurements showed that ion transfer and electron transfer are the dominant mechanisms.[9,13–16]

Recently, several studies have reported direct current generation based on forward-driven pseudocapacitors formed at the interface of ionic liquid and solid.[17–19] This effect is due to the movement of surface charges by capacitance charging/discharging at the front/end of the droplet. Also, when ionic liquid moves on the surface of reasonably porous and electrically conductive electrodes such as carbon fibers, ions are adsorbed on the surface of the oppositely charged electrode.[20,21] This phenomenon, used as a highly efficient and low-cost water purification technique is called Capacitive Deionization (CDI). Coupling capacitive deionization with forward-driven pseudocapacitance effect (i.e., pseudocapacitive deionization) should be possible by investigating the triboelectric properties of ionic liquid and porous materials such as MoS_2. MoS_2 is an excellent candidate for this purpose because of its porous structure, large specific surface area, high chemical stability, good hydrophilicity, and excellent lubricating properties.[22–26] The favorable range of

R. Ahmadi, A. Abnavi, A. Hasani, H. Ghanbari, M. R. Mohammadzadeh, F. Kabir, M. M. Adachi
School of Engineering Science
Simon Fraser University
8888 University Drive, Burnaby, British Columbia V5A 1S6, Canada
E-mail: mmadachi@sfu.ca
M. Fawzy
Department of Physics
Simon Fraser University
8888 University Drive, Burnaby, British Columbia V5A 1S6, Canada

The ORCID identification number(s) for the author(s) of this article can be found under https://doi.org/10.1002/smll.202304988

DOI: 10.1002/smll.202304988

oxidation states of Mo atoms makes MoS_2 suitable for electrosorption capacity through the pseudocapacitor reactions.[25]

In this work, we explore the triboelectric properties of an ionic liquid and 2D MoS_2 under light illumination. Specifically, we investigate the current and voltage changes that occur when a liquid droplet slides on the surface of MoS_2. Our findings reveal an intriguing phenomenon where the current and voltage increase in the forward direction and decrease in the reverse direction. We propose that this unique memory-like behavior arises from the ion adsorption/desorption processes associated with pseudocapacitive deionization/ionization at the liquid–MoS_2 interface. To support our explanation, we employ various analytical techniques including electric double layer (EDL) analysis, equivalent electrical circuit modeling, contact angle measurements, and electronic band diagrams. Moreover, we systematically analyze the influence of parameters such as velocity, step size, light wavelength and intensity, ion concentration, and bias voltage on this tribo-phototronic effect. Importantly, this behavior enables the realization of essential synaptic features, including potentiation/inhibition, paired-pulse facilitation/depression, and the transition from short-term memory (STM) to long-term memory (LTM) through mechanical stimulation. Our findings hold promising implications for the development of synaptic memory systems and intelligent sensing applications that leverage the potential of liquid–solid interfaces.

2. Results and Discussion

2.1. Measurement Setup and Material Characterizations

The measurement setup consisted of a droplet of NaCl solution that moved on the surface of 2D MoS_2 under light illumination. A schematic illustration and optical image of the measurement setup are shown in **Figure 1**a and Figure S1 (Supporting Information), respectively. A large-area MoS_2 film was synthesized on the SiO_2/Si substrate using the thermolysis technique. The illustration of the fabrication process and the optical images of the fabricated devices are shown in Figure S2a–c, (Supporting Information). The MoS_2 film consisting of nanometer-sized MoS_2 crystals was confirmed by high-resolution transmission electron microscopy (HR-TEM), where showed a honeycomb arrangement of atoms and lattice spacing of 0.27 nm (inset of Figure 1a).[27] Also, the corresponding selective-area electron diffraction (SAED) displayed hexagonally arranged diffraction spots, indicating the hexagonal lattice structure of MoS_2 crystals.[28] The Raman spectra of the MoS_2 thin film (Figure 1b) show two vibrational modes of A_{1g} (out-of-plane) at $\approx$406 cm^{-1} and $E^1{}_{2g}$ (in-plane) at $\approx$381 cm^{-1}, which are characteristic of semiconducting 2H phase MoS_2.[29] Furthermore, high-resolution X-ray photoelectron spectroscopy (XPS) spectrum confirmed the Mo $3d_{5/2}$ and S $2p_{3/2}$ doublets at 230.0 $\pm$ 0.1 and 162.0 $\pm$ 0.1 eV, respectively, which agree with previous reports on MoS_2 (Figure 1c).[30] The thickness of the MoS_2 film was $\approx$50 nm, as determined by atomic force microscopy (AFM; Figure S2d, Supporting Information). The liquid droplet was translated along the MoS_2 surface by keeping it fixed in a capillary tube and moving the substrate underneath it, using a linear motor, as schematically shown in Figure 1a. A 470 nm blue LED with a constant intensity of 20 mW cm^{-2} was illuminated on the MoS_2/liquid structure unless otherwise stated.

2.2. Triboelectric Response Between Ionic Liquid and 2D MoS_2 Under Light Illumination

Figure 1d,e shows the dynamic current–time (*I*–*t*) and voltage–time (*V*–*t*) characteristics of the device in response to five movement steps in the forward direction, followed by five movement steps in the reverse direction, returning to its initial position all while under light illumination. The velocity and the step size of the movements were 5 mm s^{-1} and 1 mm, respectively. Characterization of the motor movements is shown in Figure S3 (Supporting Information). Here, the liquid droplet is a 20 mM NaCl solution and will remain the same throughout the paper, unless stated otherwise. Each droplet movement resulted in a sharp transient peak, which decayed as a function of time until it reached a steady-state current (Figure 1d). The transient current consists of both the triboelectric and photoelectric currents, whereas the steady-state current solely originates from the photoelectric effect. Both the transient and steady-state currents increased with each forward movement of the liquid droplet on the MoS_2 film (Video S1, Supporting Information). When the direction of movement was reversed, the transient and steady-state currents decreased with each movement step, returning to its initial current value of $\approx$0.8 nA at the original position before forward movement. Similarly, the voltage response shows an increase in the transient and steady-state voltages during forward movements and a decrease in the transient and steady-state voltages during reverse movements (Figure 1e). This memory-like behavior suggests electro–optomechanical interactions between the liquid and MoS_2.[31,32]

This memory-like behavior was also observed in dark conditions where the transient current peak amplitude increased incrementally during consecutive liquid movements in the forward direction (Figure S4, Supporting Information). However, since there are no electron–hole pairs generated from the light illumination, the current consists only of the transient current generated by the triboelectric effect without the steady-state stair-case increments/decrements observed in Figure 1d. Therefore, incident light facilitates the observation of memory-like behavior by assisting the contact electrification process, elevating the overall current level, and introducing a steady-state memory behavior.

Forward liquid movements were also applied to other surfaces including an *n*-type Si wafer, *p*-type Si wafer, and SiO_2-coated Si wafer. The current measurements of the resulting liquid-*n*-type Si, liquid-*p*-type Si, and liquid–SiO_2 interfaces exhibit an approximately equal transient current peak at the onset of each liquid movement step, after which the current returns to its steady-state value (Figure S5, Supporting Information). Memory-like incremental increases in the current behavior observed in MoS_2 were not observed in these other materials.

The current–voltage (*I*–*V*) characteristics of the MoS_2 film and 20 mM NaCl solution under dark conditions demonstrate rectifying diode-like behavior, confirming the formation of a built-in potential at the interface (Figure S6, Supporting Information). This potential enables the separation of electron–hole pairs generated by bindingtons and photons, caused by the mechanical

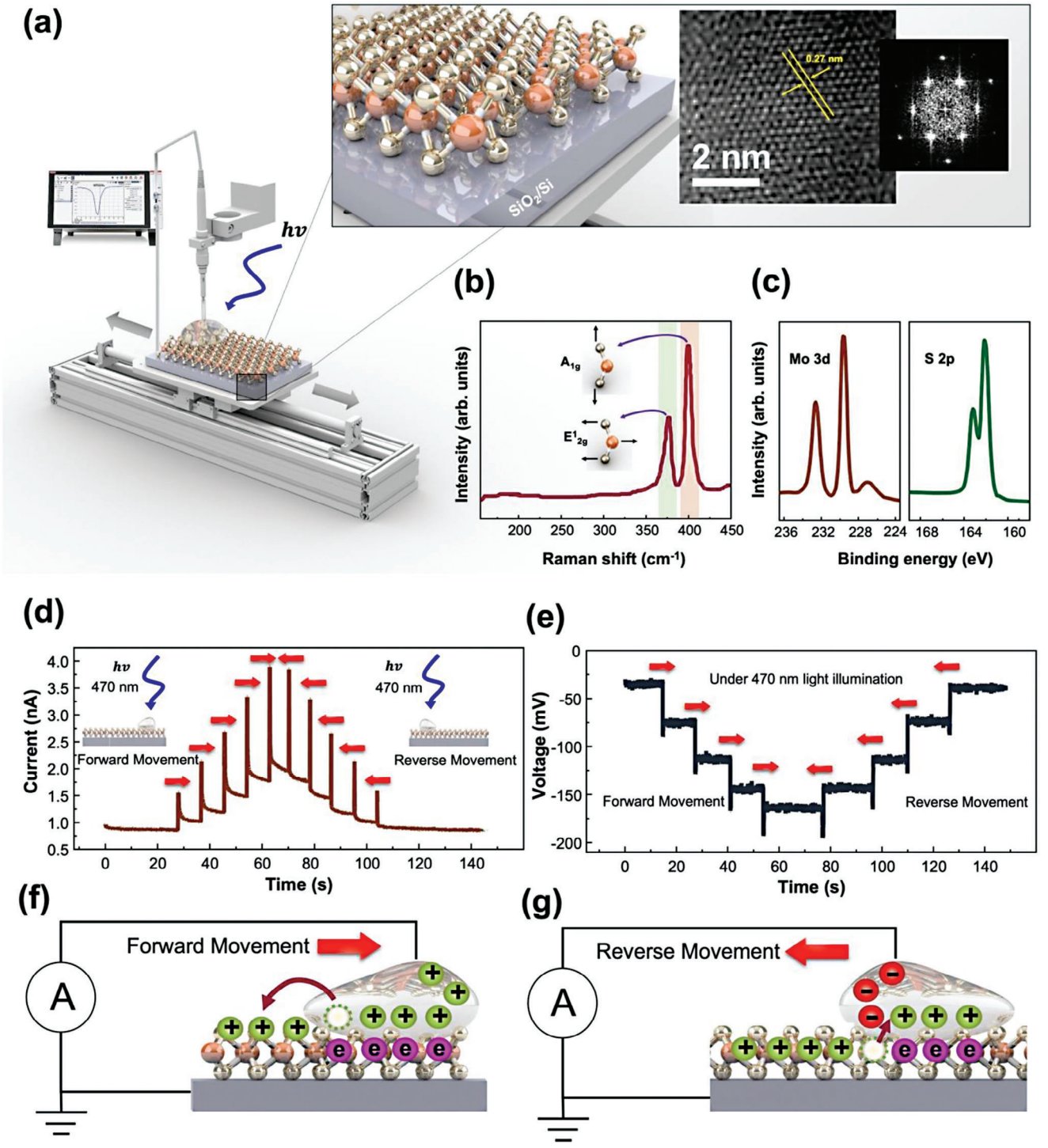

Figure 1. Triboelectric properties of the ionic liquid and MoS_2 film under light illumination. a) Schematic of the measurement setup (Inset: High-resolution transmission electron microscopy (TEM) image and the corresponding SAED pattern of the MoS_2 film). b) Raman spectrum of the MoS_2 film. c) Wide-range XPS spectra of the MoS_2 film. d) The dynamic *I*–*t* and e) *V*–*t* responses of the device for a series of five movements (step size of 1 mm) in the forward direction followed by five movements (step size of 1 mm) in the reverse direction under the radiation of 470 nm light with an intensity of 20 mW cm^{-2}. Ions are, f) adsorbed to the MoS_2 surface in forward movement and, g) desorbed from the surface due to the reverse polarity of the front-end pseudocapacitors formed between the liquid and MoS_2.

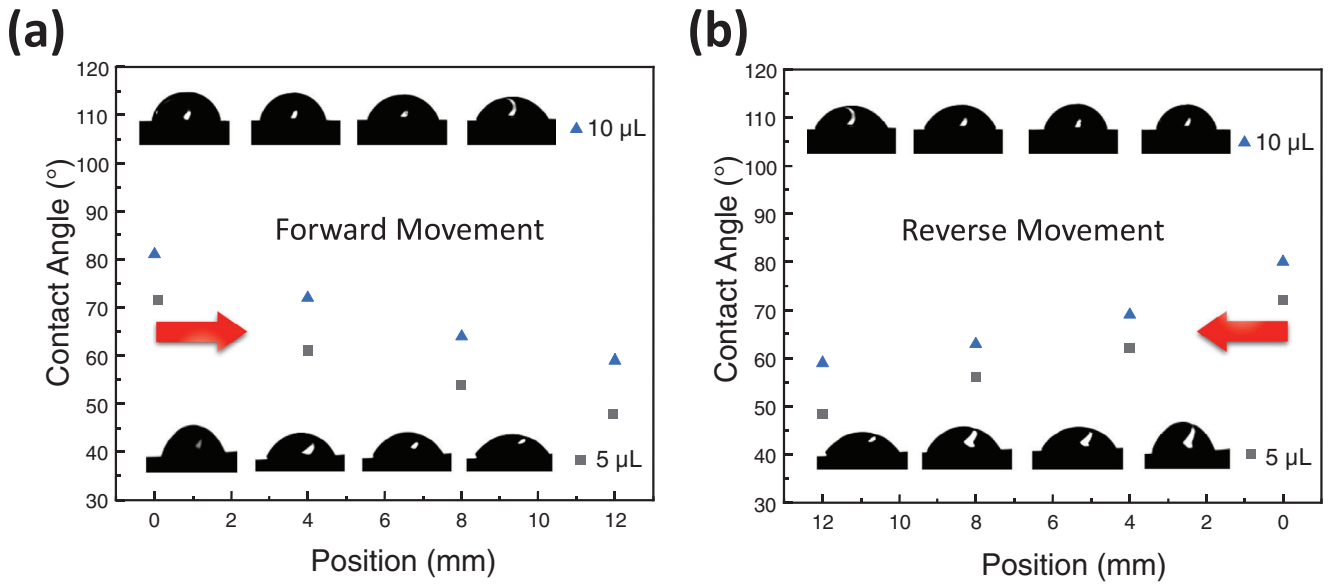

Figure 2. Contact angle measurements for two droplets with volumes of 5 and 10 µL. a) The contact angle decreases during the forward movement steps of the liquid droplet and b) the contact angle increases during subsequent reserve movements and returns to the original contact angle at the starting position (0 mm). The increasing/decreasing contact angle is attributed to ion adsorption/ desorption to/from the MoS_2 surface.

movement of liquid on solid and light irradiation, respectively. Also, MoS_2 has been shown to have a high Volume Adsorption Capacity (VAC) owing to its rapid ion transfer, making it a suitable candidate for capacitive water deionization.[24] As the NaCl solution moves on the MoS_2 surface, a pseudocapacitance forms at the front end of the droplet, and Na^+ ions are adsorbed or trapped on the surface of MoS_2 (Figure 1f).[17,19,21] To verify the crucial role of the interface traps, water movement experiments were repeated on MoS_2 films passivated with a thin film of Al_2O_3.[33] The surface passivation resulted in nearly equal-amplitude current peaks during each movement in the forward and reverse directions, similar to the liquid-Si and liquid-SiO_2 interfaces, and exhibited no memory-like behavior (Figure S7, Supporting Information). The reduction of Na+ ions in the liquid during forward movements leads to increasing triboelectric (transient peak) and photoelectric (steady-state) currents in each subsequent movement step. Similar increases in current have also been observed in NaCl solution-semiconductor/dielectric junctions when the concentration of the NaCl solution was decreased.[8,14,16] In the reverse movements, the solution encounters a positively charged surface resulting in the accumulation of the negative ions at the front end and reversing the polarity of the pseudocapacitor (Figure 1g). This polarity reversal causes positive ion desorption from the MoS_2 surface. Hence, the liquid regains the positive ions, and both triboelectric and photoelectric currents decrease during movements in the reverse direction. Eventually, the current returns to its starting value (≈0.8 nA) when the droplet reaches its starting position.

The effect of MoS_2 film thickness was also investigated under the same measurement conditions (1 mm movement step size, 5 mm s^{-1} velocity, λ = 470 nm incident light at 20 mW cm^{-2}, 20 mM NaCl liquid droplet). The *I–t* response for three different film thicknesses of 16.5, 22, and 115 nm, shows that the current level decreases with increasing the thickness of MoS_2 (Figure S8, Supporting Information). It has been demonstrated that thicker MoS_2 has a higher surface potential barrier and resistivity.[34] Therefore, by increasing the thickness of MoS_2, ions must overcome a higher barrier to transport on the MoS_2 film that results in a lower current level. Also, due to the abundance of vacancies in the MoS_2 films, the memory-like behavior of the movements is still observable in all of the thicknesses. Moreover, the same measurement was also repeated with a different substrate (Al_2O_3/Si) and the response exhibited the same behavior as MoS_2/SiO_2/Si devices, thereby excluding the effect of the underlying substrate (Figure S9, Supporting Information).

2.3. Contact Angle Measurements

To further analyze the ion adsorption on the MoS_2 film, contact angle measurements for two liquid droplet volumes of 5 and 10 µL were performed. The photograph of the measurement setup is shown in Figure S10 (Supporting Information). The contact angle between the 10 µL liquid droplet and MoS_2 at the initial position (x = 0) was measured to be ≈81°. Then liquid droplet was moved in the forward direction to positions of x = 4, 8, and 12 mm, and the contact angles decreased to ≈73°, ≈65°, and ≈60°, respectively (**Figure 2**a). There are two factors contributing to this behavior that are intrinsically related to the interaction between the liquid and MoS_2. First, it has been shown that applying positive gate voltage can significantly decrease the contact angle due to the stronger interaction between liquid and solid.[35] Since there is no applied voltage in our case, the built-in potential governs the liquid–MoS_2 interface. Hence, a smaller contact angle suggests a higher built-in potential. Second, the contact angle has been shown to decrease with a decrease in the NaCl concentration due to the adsorption of ions at the solid surface.[36,37] Following the forward movement steps, the liquid droplet was

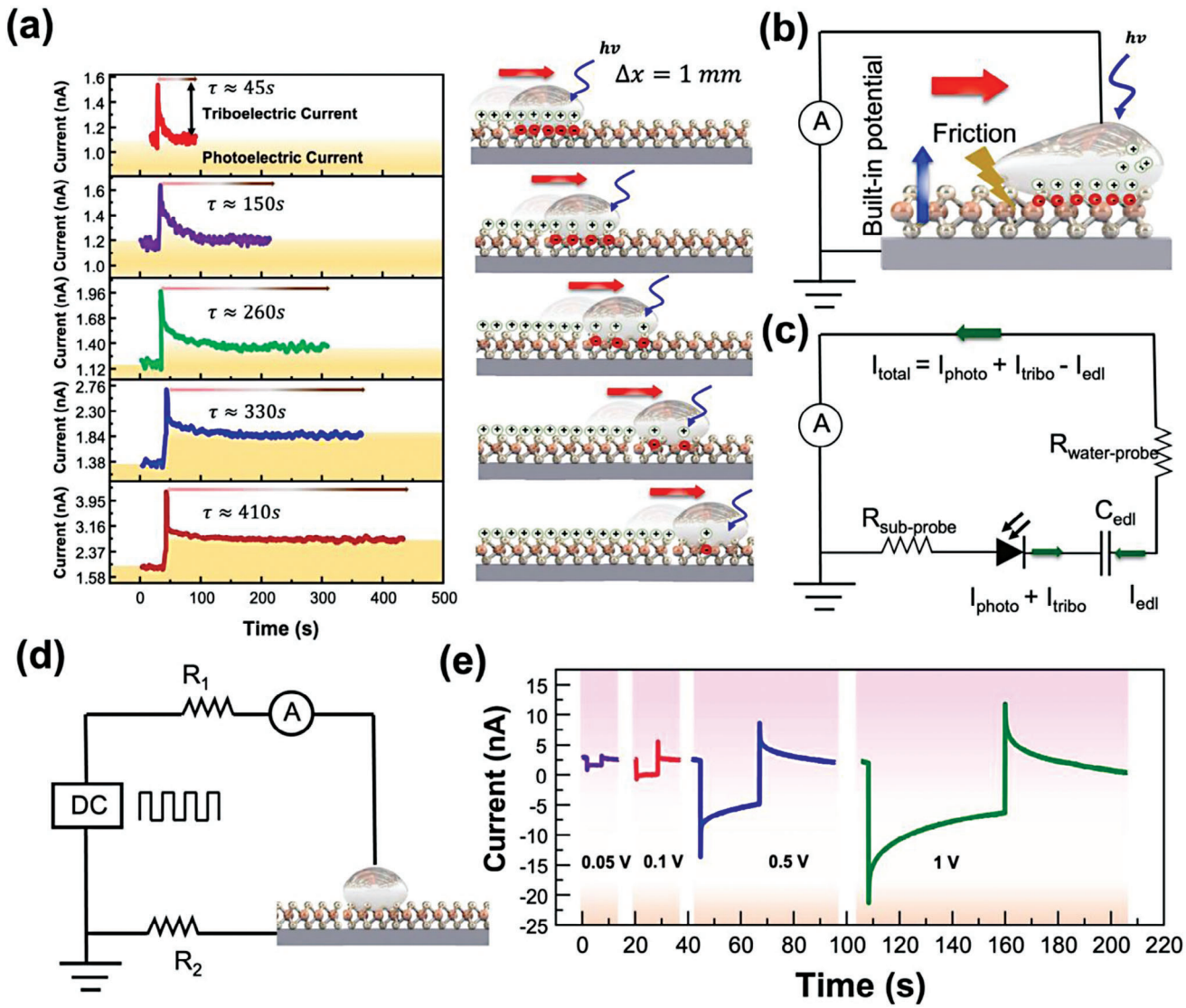

Figure 3. Circuit model of the mechanism. a) Current–time (*I*–*t*) response of the MoS_2-liquid heterojunction during consecutive forward movements, each with an equal step size of 1 mm. As the droplet moves forward, positive ions are adsorbed on the surface resulting in a larger built-in potential and smaller EDL. b) Schematic of the device under light illumination. c) Equivalent circuit of the device. The total current is the sum of the photocurrent and EDL capacitance discharge current. d) A second circuit diagram to investigate the effect of applying external square-wave voltage cycles to a stationary device analogous to the liquid movement behavior, and e) the corresponding *I*–*t* response. A higher voltage resulted in higher peaks, higher steady-state, and longer relaxation times (the same function as the built-in potential).

moved in the reverse direction, during which it retained its contact angle values of ≈64°, ≈70°, and ≈80° at $x = 8$, 4,and 0 mm, respectively (Figure 2b). These measurements further indicate the increase and decrease in the built-in potential due to ion adsorption and desorption at the MoS_2 surface during the forward and reverse movements, respectively.

The 5 µL droplet exhibited the same trend of decreasing contact angle during forward movements, followed by increasing contact angle during reverse direction movements. However, the 10 µL droplet had a higher contact angle than the 5 µL droplet that could be due to the larger contact radius.[38] During the contact angle measurements, a capillary tube was used to hold, drag, and release the droplet. Therefore, the shape of the droplet remained constant before and after movement with the capillary tube (Figure S11, Supporting Information).

2.4. Circuit Model of the Mechanism

Moving the liquid droplet on the MoS_2 surface results in the generation of triboelectric and photoelectric currents. **Figure 3**a shows the *I*–*t* characteristics of a moving water droplet on the MoS_2 film with different positions and the same step sizes. Longer distances from the starting position led to higher peak amplitudes and longer relaxation times in the triboelectric current, and higher amplitude in the photoelectric current. The

schematic representation of the moving liquid on the MoS_2 film under light illumination and its equivalent electrical circuit diagram are shown in Figure 3b,c, respectively. When the liquid moves on the MoS_2 film, the EDL capacitance generates $I_{edl} = C_{edl} \frac{dv_{edl}}{dt}$, where C_{edl} is the EDL capacitance and v_{edl} is the EDL potential across the interface. This current is in the opposite direction of the liquid-MoS_2 diode photocurrent (I_{ph}) due to the cathodic behavior of n-MoS_2.[39] Therefore, the total current is $I_{total} = I_{ph} - I_{edl}$. The ion adsorption along the MoS_2 film consequently decreases the EDL capacitance and I_{edl}. Hence, as the liquid moves in the forward direction, the contribution of I_{edl} to the total current reduces resulting in a longer relaxation time (τ) to reach the steady-state current (Figure 3a). To further investigate this observation, we assembled a second circuit (Figure 3d), where the interface potential was forced by an external bias voltage pulse while C_{edl} was kept constant on a stationary droplet. Analogous to the larger distance of the liquid to its initial position in Figure 3a, by increasing the magnitude of the external bias square-wave voltage pulse amplitude from 0.05 to 1 V, both the transient and steady-state currents increase, and takes a longer time for the currents to relax (Figure 3e).

The movement of the surface charges by pseudocapacitance charging/discharging at the front/end of the liquid–solid interface results in direct current generation. A different electrode configuration, where metal contacts were both placed on the MoS_2 film, was investigated to show this charging/discharging effect and no memory-like behavior was observed (Figure S12, Supporting Information). The forward movement steps induced a positive current, whereas reverse movement steps induced a negative current, similar to a previous report on monolayer MoS_2.[19] This phenomenon can be also explained by our proposed reversed-polarity model in the forward and reverse directions. As shown in Figure S13a (Supporting Information), as the droplet moves forward, the distribution of cations in the droplet causes electrons to flow from the right to the left in the circuit. In the opposite direction, the asymmetrical distribution of anions in the droplet reverses the flow of electrons (Figure S13b, Supporting Information).

2.5. Current–Voltage (*I–V*) Behavior and Electronic Band Diagrams

The proposed mechanism can be discussed using steady-state *I–V* measurements and band diagrams of the liquid and MoS_2 interface. The steady-state *I–V* curves measured after five consecutive movement steps, each with a step size of 1 mm, are shown in **Figure 4**a. During droplet movement in the forward direction, both the short-circuit current (I_{sc}) and open-circuit voltage (V_{oc}) increase (Figure 4b). The droplet movement in the reverse direction resulted in decreasing I_{sc} and V_{oc} (Figure 4c). Relatively high photocurrent and photovoltage of this structure suggest excellent photovoltaic properties that can be further improved upon movement in the forward direction. Accordingly, photocurrent responsivity (R_I) and photovoltage responsivity (R_v) were calculated as $R_I = \frac{I_{ph}}{P \times S}$, and $R_v = \frac{V_{ph}}{P \times S}$ where I_{ph}, V_{ph}, P, and S are photocurrent, photovoltage, light intensity, and the active area, respectively. Here, the illuminated light has a wavelength of 470 nm with an intensity of 20 mW cm^{-2}. The active area is considered the area covered by the liquid droplet, which is $3.14 \times (0.5)^2 = 0.785$ mm^2. The R_V and R_I measured as a function of position during consecutive forward movements are shown in Figure S14 (Supporting Information). Both R_v and R_I increase as water moves forward reaching the highest values of 15.74 nA mW^{-1} and 1.05 V mW^{-1}, respectively.

Schematic diagrams of the five stages of two consecutive droplet movements are shown in Figure 4d. These stages consist of three static stages and two dynamic stages. In the static stages, current is generated only due to the photoelectric effect while in the dynamic stages, both photoelectric and triboelectric effects contribute. The corresponding band diagrams for each stage are shown in Figure 4e. MoS_2 synthesized by thermolysis has good crystalline quality,[40] which results in fewer S deficiencies and weakly n-doped MoS_2 films.[41,42] Therefore, the Fermi level of MoS_2 is expected to be lower than that of the NaCl solution that causes downward bending upon contact.[43] Because of the liquid pressure of the droplet on the MoS_2 surface, the electrons of the NaCl solution interact with the electrons at the MoS_2 surface, which may lead to an overlap of the electron clouds and electron transfer from the NaCl solution to MoS_2.[8]

In the first stage (i), where the liquid is stationary and illuminated by light, photons can generate excitons in MoS_2, and the built-in potential separates electrons from holes, resulting in a photoelectric current (static photoelectric current). As the liquid moves on the MoS_2 surface (ii), more excitons are generated owing to the contribution of bindingtons, bond formations, and ion transfer,[44] resulting in a transient current peak. In addition, positive ions are adsorbed on the surface of MoS_2 causing an increase in the built-in potential between the liquid and MoS_2, a higher static photoelectric current in the third stage (iii), and a higher transient current in the fourth stage (iv). Similarly, due to the loss of more ions during the second movement (v), the built-in potential and the static photoelectric current increase further (Figure 3a).

2.6. Current Response Under Different Conditions

The tribo-phototronic behavior was measured under various conditions. For instance, increasing the velocity of the mechanical pulse (5, 10, 20, and 50 mm s^{-1}) with the same step size of 1 mm increased the transient current amplitude (**Figure 5**a). A higher velocity generated a larger triboelectric response, which is due to the generation of more bindingtons, while the steady-state current remained approximately the same at each velocity owing to the same built-in potential. Increasing the step size (1, 2, 5, 10, 20, and 30 mm) while maintaining a constant velocity of 5 mm s^{-1} increased both transient and steady-state currents (Figure 5b). This is due to more ion adsorption and a higher built-in potential at longer movement distances. Voltage–time measurements as a function of step size showed that increasing the step size results in higher open circuit voltage (Figure S15a, Supporting Information), which is closely related to the built-in potential.[45] Increasing the velocity of the droplet movement caused the open circuit voltage to decrease only slightly (Figure S15b, Supporting Information). This suggests a slightly lower built-in potential was generated upon faster movements that may be due to less time for the absorption events.

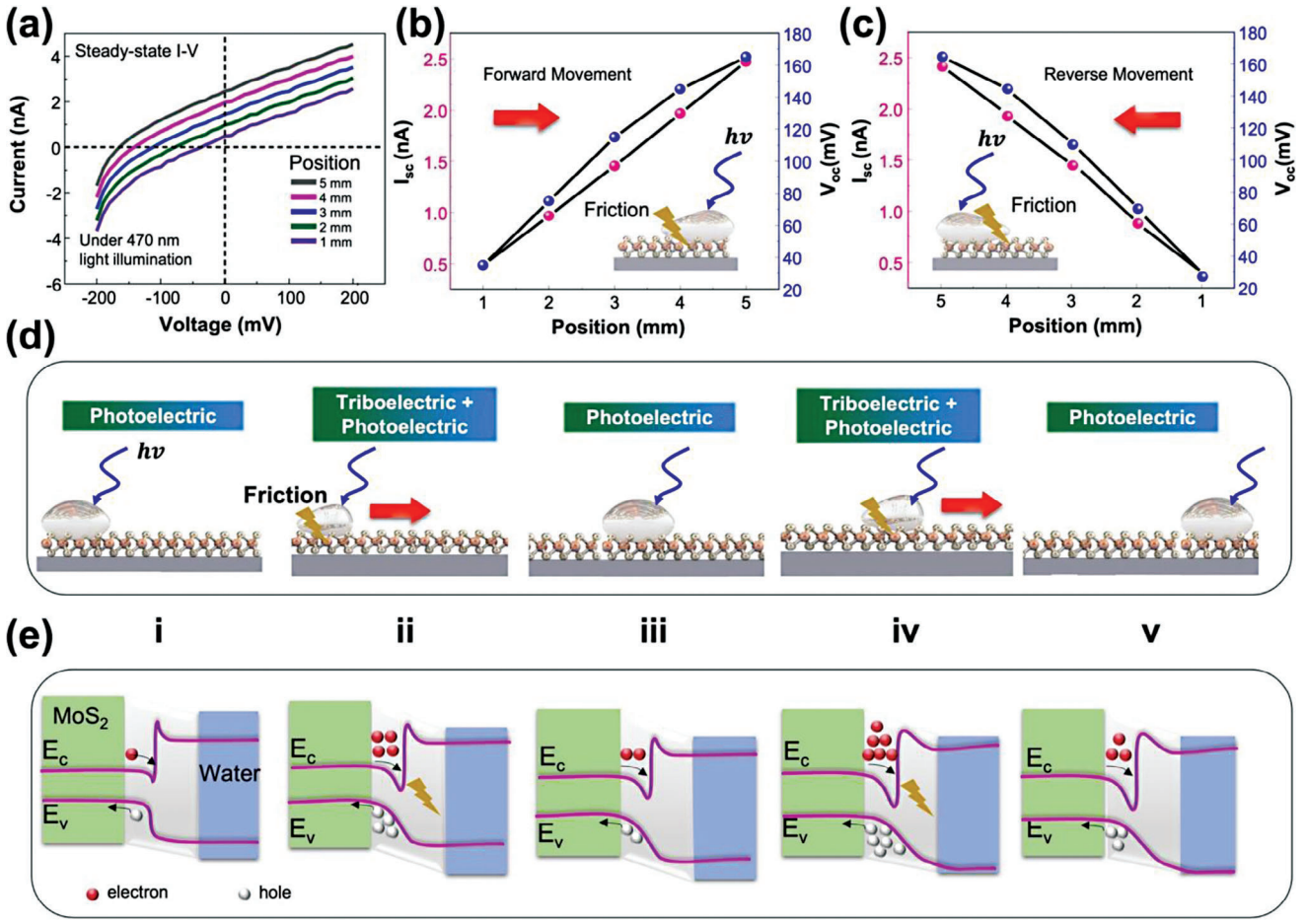

Figure 4. Steady-state *I–V* curves and band diagrams. a) Steady-state *I–V* response measurements obtained at positions 1, 2, 3, 4, and 5 mm (five consecutive droplet movements with step size of 1 mm each) in the forward direction. I_{sc} and V_{oc} versus position for b) forward, and c) reverse movements. d) Schematics of five different stages (static-movement-static-movement-static) of two consecutive movements and, e) their corresponding electronic band diagrams.

Incident light facilitates the observation of the tribo-phototronic synaptic plasticity between the liquid and MoS_2 by generating more photon-excited electron–hole pairs. The current responses of the forward movements under illumination at different wavelengths (400, 450, 500, 600, 700, and 800 nm) at a constant intensity of 100 μW cm^{-2}, step size (1 mm), and velocity (5 mm s^{-1}) are shown in Figure 5c. The maximum current is generated at the wavelength of 450 nm. The reflectance spectrum of liquid-MoS_2 (Figure S16, Supporting Information) showed minimum and maximum reflection at the wavelengths of ≈450 nm, and ≈780 that is similar to the reflection spectrum of water.[46] Also, it has been demonstrated that MoS_2 has the maximum absorption at ≈450 nm that increases the photon-excited electron–hole pairs.[47] Increasing the intensity of light from 1 to 30 mW cm^{-2} enhances the electron–hole generation, increasing the steady-state photoelectric-generated current amplitude whereas the transient triboelectric-generated current remains approximately the same at each intensity (Figure 5d). Because of the screening effect, the photocurrent responsivity decreased at higher intensities.[48]

The concentration of NaCl plays a crucial role in the formation of the built-in potential and EDL. Five droplets of different NaCl concentrations (0.2, 20, 200, 500, and 1000 mM) were prepared and placed on the MoS_2 surface. The forward movement steps of the 20 mM solution generated the highest current level, whereas the tribo-phototronic synaptic plasticity behavior diminished at higher concentrations (Figure 5e). Higher concentrations may create a thicker EDL at the interface, thereby reducing both the triboelectric and photoelectric components of the current response. Note that, unlike NaCl solutions, the triboelectric and photoelectric currents of DI water and MoS_2 fluctuated over time. This could be due to the fact that water adsorbs ions from the environment, and by introducing a dominant ion such as NaCl, the measurements are more consistent and repeatable over time. The transient and steady-state current values for 20 measurements are shown in Figure S17 (Supporting Information). Both current level values increase from measurement to measurement up to a peak value followed by decreases in current. The increases in current are attributed to ion adsorption from the environment and the decrease in current during later measurements may be due to water evaporation.

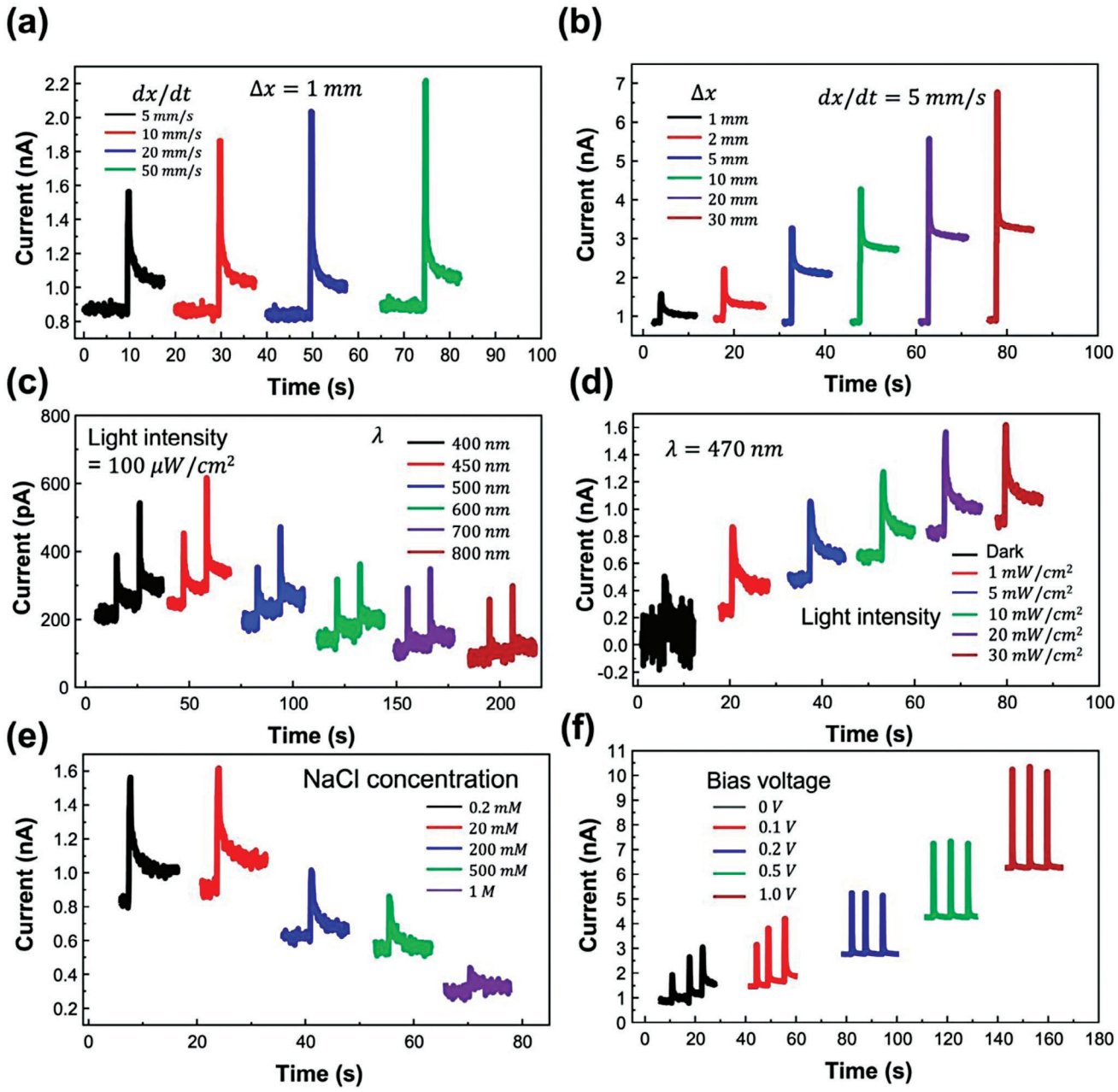

Figure 5. Tribo-phototronic current under different conditions. *I–t* response of one forward movement of NaCl solution on the MoS_2 film with a) different velocities of 5, 10, 20, and 50 mm s^{-1} and b) different step sizes of 1, 2, 5, 10, 20, and 30 mm. *I–t* response of forward movements of the NaCl solution on the MoS_2 film under illumination at c) 400, 450, 500, 600, 700, and 800 nm (intensity = 100 μW cm^{-2} in each case) and d) at different light intensities of 1, 5, 10, 20, and 30 mW cm^{-2} (λ = 470 nm). e) *I–t* response of one forward movement of a droplet with NaCl concentrations of 0.2, 20, 200, 500, and 1000 mM on the MoS_2 film. f) Effect of reverse bias voltages of 0, 0.1, 0.2, 0.5, and 1.0 V on the current response of three consecutive forward movements.

Finally, the application of an external reverse bias voltage can enhance electron–hole separation and collection (Figure 5f). Four different reverse bias voltages (0.1, 0.2, 0.5, and 1 V) were applied to the device during the forward step movements. The low bias voltage of 0.1 V is not high enough to dominate the charge collection, and incremental increases in current during each movement step are observable. At higher bias voltages (0.2, 0.5, and 1 V), the triboelectric and photoelectric current amplitudes increased, but the applied bias also overruled the built-in potential and eliminated the incremental increase in current behavior.

2.7. Artificial Synapse Application

A synapse in the human brain is a small physical gap where a signal is passed from one signal-passing neuron, known as a

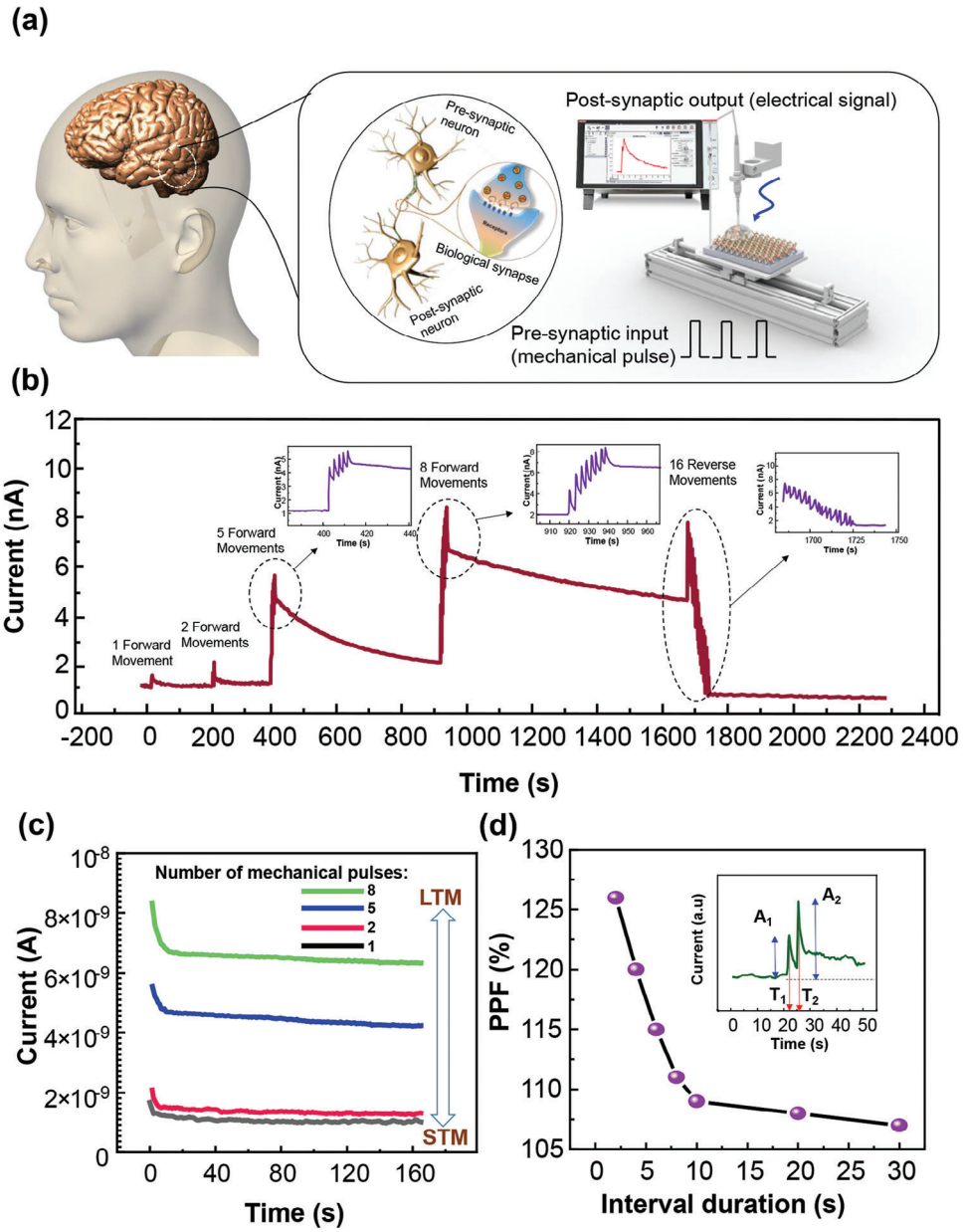

Figure 6. Artificial synapse characteristics. a) Schematic of a biological synapse in the human brain and liquid-MoS_2 as an artificial synapse where the mechanical movement is the pre-synaptic input and electrical signal is the post-synaptic output. b) *I–t* measurements for 1, 2, 5, and 8 consecutive forward movements as the writing steps followed by 16 reverse movements to the initial position as the erasing steps. The forward and reverse pulses had 1 mm of duration, 2 s of time intervals, and an intensity of 5 mm s^{-1}. c) *I–t* measurements after 1, 2, 5, and 8 mechanical pulses show the transition from STM to LTM. d) PPF index versus interval duration between two consecutive mechanical pulses. The inset shows the I-t response of two consecutive pulses.

pre-synaptic neuron, to another, known as a postsynaptic neuron (**Figure 6**a).[49] Synaptic plasticity refers to activity-dependent changes in synaptic transmission and is the principal mechanism of memory and learning. Synaptic plasticity behaviors, such as Short-Term Plasticity (STP), and Long-Term Plasticity (LTP) are key components for perception, discretion, and learning functions that are difficult to realize with von Neumann architectures. Electrically, optically, ferroelectrically, magnetically, and mechanically modulated synaptic plasticity have been investigated by researchers to overcome von Neumann barriers.[49–54] In tribo-phototronic MoS_2-liquid heterostructures, an artificial optomechanical synaptic behavior where electrical current is the post-synaptic signal, and the mechanical movements act as pre-synaptic signals, can be realized (Figure 6a).

In this artificial synapse, the velocity and step size of the motor serve as the intensity and duration of the pre-synaptic signals. The excitatory post-synaptic current (EPSC) signals as a function of intensity (i.e., velocity) at a fixed duration (i.e., step size)

and vice versa are shown in Figures 5a,b, respectively. Figure 6b shows the *I–t* response for 1, 2, 5, and 8 sequential forward movements, which function as writing steps, each separated by a long delay. For a single forward movement, the current returned to its steady-state value after ≈50 s, but the current decayed more slowly as the number of sequential movement steps increased. The STM to LTM transition is shown in Figure 6c when the number of mechanical pulses increases from 1 to 8. As explained earlier, the transition from STM to LTM is due to the larger built-in potential and smaller EDL capacitance upon further movement. When eight consecutive pulses were applied, the current decayed the slowest. The forward movements were followed by 16 sequential reverse movements returning to the original position, which functioned as erasing steps. In other words, the stored information is erased if the droplet returns to its initial position along the same path. During the reverse direction movement, the adsorbed ions are released and the liquid collects the lost ions and reaches its initial concentration.[24] The paired-pulse facilitation (PPF) index is denoted in the inset of Figure 6d as the ratio of A_2 to A_1 (A_2/A_1), where A_1 and A_2 are the current amplitudes from two successive pulses with an interval time of $\Delta t = T_2 - T_1$. The current amplitude generated by the second pulse is consequently greater than that of the first pulse if the PPF index is greater than 1. The pulse interval, which is determined by the amount of time between two consecutive spikes, increased from 2 to 30 s, with the pulse interval of 2 s having the highest PPF index (≈126%) (Figure 6d). Higher interval times allow the EDL to relax and suppress the increase in the built-in potential in the following pulse, resulting in a lower PPF compared to shorter intervals. Finally, the stability of the device in over ≈140 write-erase cycles is shown in Figure S18 (Supporting Information). Both the triboelectric and photoelectric currents are subject to a slight decrease, which may be attributed to environmental factors such as permanent ion deposition on the surface and liquid evaporation.

Mechanical-stimulated artificial synapses are a relatively new area of research and development in the field of neuromorphic computing. These synapses represent a transition from traditional electronic synapses by relying on mechanical forces or movements instead of electrical or chemical signals.[53,55] They can facilitate spatiotemporal input recognition that is an important neuron functionality.[56] Unlike their electronic counterparts, mechanical synapses have the potential to operate with significantly lower energy consumption, which is crucial for developing sustainable and power-efficient computing systems.[55] In our device, ionic liquid and MoS_2 form a network of self-powered neurons that are activated upon contact and there is no need to apply a bias voltage to retain the state. This non-volatility characteristic not only reduces energy requirements but also aligns with the way our brains maintain synaptic strength over time. In terms of robustness, liquid-MoS_2 exhibits inherent durability and resilience that makes it less susceptible to environmental factors such as electromagnetic interference and radiation. Lastly, this structure may be suited for integration with biological systems or medical devices, opening up new prospects toward intelligent liquid–solid applications such as iontronics, biosensors, electronic eyes, gas sensors, and digital microfluidics.[41,46,57–60]

In addition to MoS_2, tungsten disulfide (WS_2) is another important example of TMDCs with promising electronic, optical, mechanical, and chemical properties.[61–64] Using the same method as MoS_2, we fabricated large-area 2D WS_2 (see Experimental Section) and conducted triboelectric measurements under light illumination.[65] The XRD and XPS characterizations shown in Figure S19a–c (Supporting Information) confirm the successful formation of WS_2 on Si/SiO_2. A 20 mM NaCl liquid droplet was moved forward in three steps (1 mm each with a velocity of 5 mm s^{-1}) and reversed to the initial position on the WS_2 film under light illumination. The results show that the tribo-phototronic properties of liquid-WS_2 exhibit the same behavior as liquid-MoS_2, i.e., increasing and decreasing responses with forward and reverse movements, respectively (Figure S19d, Supporting Information). Therefore, the tribo-phototronic synaptic plasticity behavior can be extended to liquid-WS_2 heterojunction.

Liquid–solid interfaces have been shown to have remarkable properties with applications in a variety of research areas. To the best of the authors' knowledge, modern scientific research on this interface started with the streaming potential effect, which is used in supercapacitors, self-powered nanosystems, and electrokinetic flowmeters.[66–69] Ion-sensitive field-effect transistors, electrochemical photolysis, and capacitive deionization were among the greatest discoveries of the 20th century surrounding liquid–solid interface.[70–72] More recently, the forward-driven pseudocapacitance effect between ionic liquids and solids (Graphene and MoS_2) has been utilized to generate direct current. Wang et. Al. introduced liquid–solid-based energy harvesters for the first time and later quantified the charge transfer between liquids and solids.[16–17,73] In this work, based on the tribo-phototronic writeable and erasable behavior, we proposed an artificial synaptic application based on the liquid–solid interface.

3. Conclusion

In summary, we investigated the coupling between the forward-driven pseudocapacitance effect and capacitive deionization at the ionic liquid–MoS_2 interface. When the ionic liquid moved in the forward direction on the MoS_2 surface under light illumination, the current flowed from MoS_2 to the liquid. This current increased during forward movements and decreased during reverse movements, returning to the original current value at the original movement position. This behavior was attributed to the modulation of the built-in potential due to pseudocapacitive ionization/deionization. It was further described using contact angle measurements, electronic band diagrams, EDL, and an equivalent electrical circuit. Also, the effects of multiple conditions such as movement distance and velocity, light wavelength and intensity, ion concentration, and bias voltage were studied. Finally, a synaptic memory based on this effect was suggested. This mechanically stimulated synapse could imitate the main brain functions such as potentiation/inhibition, paired-pulse facilitation/depression, STM, and LTM.

4. Experimental Section

MoS_2 Thin Film Synthesis: SiO_2 (300 nm)/Si (and Al_2O_3 (100 nm)/Si) wafers were cleaned using a conventional cleaning procedure, followed by ultrasonication in acetone, isopropyl alcohol, and deionized (DI) water. To obtain hydrophilic surfaces on the SiO_2/Si wafers, O_2 plasma surface

treatment was performed for 15 min. The precursor solutions were prepared by dissolving $(NH_4)_2MoS_4$ powder (Sigma-Aldrich, 99.97% purity) in ethylene glycol (Sigma–Aldrich, 99.8% purity, anhydrous) at concentrations of 100 mM, 200 mM, 500 mM, and 1 M corresponding to MoS_2 film thicknesses of 16.5, 22, 50, and 115 nm, respectively. The precursor solution was spin-coated onto the prepared SiO_2/Si (Al_2O_3/Si) substrate at 3500 rpm for 60 s. High-purity N_2 gas was used for the thermolysis process in a thermal CVD system. First, the CVD chamber temperature was increased to 500 °C and maintained at this temperature for 30 min under flowing N_2 at 1 Torr. The flow rate of N_2 was set to 200 cm^3 min^{-1} using mass flow controllers. The temperature of the CVD furnace was then increased to 950 °C and maintained for 1 h. Sulfur sublimation was initiated by placing sulfur powder (Sigma–Aldrich, 99.5% purity) in the heating zone, which was set to 300 °C.

WS_2 Film Synthesis: SiO_2/Si substrates were cleaned and treated with O_2 plasma for 15 min to make them hydrophilic. The substrates were then coated with 10 mM ammonium tetrathiotungstate $(NH_4)_2WS_4$ (Sigma–Aldrich, 99.9% purity) dispersed in ethylene glycol using a spin coater at 3500 rpm for 60 s. The samples were placed on a heated plate at 50 °C for 15 min to eliminate the solvent. To begin the thermolysis process, the substrates were placed in a quartz tube chamber. During this process, pure N_2 (200 cm^3 min^{-1}) was introduced into the chamber. Initially, the temperature was increased to 500 °C and maintained for 30 min. Under N_2 gas, the chamber pressure was held at 1.2 Torr. The temperature was then increased to 900 °C and held there for 1 h. In a different annealing zone, sulfurization was initiated with 0.6 g of 99.5% sulfur powder (Sigma–Aldrich) and continued for 1 h at this temperature.

Material Characterization: High-resolution transmission electron microscopy (HR-TEM) was performed using a JEOL-2100F instrument to confirm the quality of the MoS_2 crystal. The Raman spectra of the continuous MoS_2 film were recorded on a Renishaw inVia confocal Raman microscope equipped with a 514 nm continuous-wave excitation laser. Kratos X-ray photoelectron spectrometer (Axis Ultra DLD, Kratos Analytical, England) was used to conduct X-ray photoelectron spectroscopy (XPS) with Mg K radiation (1250 eV) and a constant pass energy of 50 eV in a vacuum of 1×10^{-5} mbar. X-ray diffraction (XRD) analysis (D8-Advance, Bruker-AXS, Germany) with a Cu K target at 0.1542 nm was used to ascertain the crystal structures of the MoS_2 and WS_2 thin films. To determine the thickness of the MoS_2 films, atomic force microscopy (AFM, Asylum MFP3D) was used.

Triboelectric Measurements: The liquid droplets were controlled using a capillary tube with a diameter of 1 mm. A copper wire through the capillary tube was in contact with the liquid droplet and served as the first electrode. The distance between the capillary tube and the MoS_2 surface was ≈2 mm. The Cr/Au (10/60 nm) electrode was deposited on the MoS_2 surface using a thermal evaporation system. The MoS_2 was grounded, and a Keithley 2400 *I–V* measurement tool was used for real-time data collection. A motorized linear stage was used to move the MoS_2 substrate while the capillary tube held the droplet. The velocity and step size of the motor could be precisely controlled. The MoS_2-liquid structure was always under light illumination (470 nm LED, 20 mW cm^{-2}), and the liquid was 20 mM NaCl unless otherwise noted.

Supporting Information

Supporting Information is available from the Wiley Online Library or from the author.

Acknowledgements

This work was funded by the Natural Sciences and Engineering Research Council of Canada (NSERC) (RGPIN-2017-05810 and CRDPJ 522672 – 17) and the Western Economic Diversification Canada (WD) Project No. 000015280. The authors thank B. Kim for the maintenance of the SFU Engineering Science cleanroom facility and Dr. D. Leznoff for access to Raman Spectroscopy instrumentation. The authors acknowledge 4D LABS facilities that facilitated the XPS and XRD measurements.

Conflict of Interest

The authors declare no conflict of interest.

Author Contributions

R.A. and A.A. contributed equally to this work. M.M.A. supervised the project. R.A. and A.A. performed all experimental design and measurements under the supervision of M.M.A.. A.H. designed the figure schematics, prepared the WS_2 films, and performed HRTEM, XPS, and XRD. H.G. prepared the MoS_2 films, performed atomic layer deposition, and participated in the theoretical discussions. M.R.M. performed Raman spectroscopy and participated in the data analysis. M.F. and F.K. contributed to the execution of this project and participated in the data analysis and discussions. R.A. and A.A. wrote the manuscript. M.M.A. revised the manuscript. All authors discussed the results, read the manuscript, and agreed with its content.

Data Availability Statement

The data that support the findings of this study are available from the corresponding author upon reasonable request.

Keywords

liquid–solid interface, MoS_2, pseudocapacitance, synaptic plasticity, triboelectric

Received: June 13, 2023
Revised: October 27, 2023
Published online:

[1] X. Shi, K. Ueno, T. Oshikiri, Q. Sun, K. Sasaki, H. Misawa, *Nat. Nanotechnol.* **2018**, *13*, 953.
[2] X. Tang, W. Li, L. Wang, *Nat. Nanotechnol.* **2021**, *16*, 1106.
[3] Y. Zeng, Y. Luo, Y. Lu, X. Cao, *Nano Energy* **2022**, *98*, 107316.
[4] X. Li, J. Tao, X. Wang, J. Zhu, C. Pan, Z. L. Wang, *Adv. Energy Mater.* **2018**, *8*, 1800705.
[5] Y. Chen, B. Xie, J. Long, Y. Kuang, X. Chen, M. Hou, J. Gao, S. Zhou, B. Fan, Y. He, Y.-T. Zhang, C.-P. Wong, Z. Wang, N. Zhao, *Adv. Mater.* **2021**, *33*, 2104290.
[6] Y. Yan, X. Zhou, S. Feng, Y. Lu, J. Qian, P. Zhang, X. Yu, Y. Zheng, F. Wang, K. Liu, S. Lin, *J. Phys. Chem. C* **2021**, *125*, 14180.
[7] M. Zheng, S. Lin, L. Zhu, Z. Tang, Z. L. Wang, *Adv. Mater. Interfaces* **2022**, *9*, 2101757.
[8] S. Lin, X. Chen, Z. L. Wang, *Nano Energy* **2020**, *76*, 105070.
[9] M. Zheng, S. Lin, Z. Tang, Y. Feng, Z. L. Wang, *Nano Energy* **2021**, *83*, 105810.
[10] P. Yang, Y. Shi, S. Li, X. Tao, Z. Liu, X. Wang, Z. L. Wang, X. Chen, *ACS Nano* **2022**, *16*, 4654.
[11] Y. Shi, P. Yang, R. Lei, Z. Liu, X. Dong, X. Tao, X. Chu, Z. L. Wang, X. Chen, *Nat. Commun.* **2023**, *14*, 3315.
[12] R. Lei, S. Li, Y. Shi, P. Yang, X. Tao, H. Zhai, Z. L. Wang, X. Chen, *Adv. Energy Mater.* **2022**, *12*, 2201708.
[13] S. Lin, Z. Lin Wang, *Mater. Today* **2023**, *62*, 111.
[14] J. Nie, Z. Ren, L. Xu, S. Lin, F. Zhan, X. Chen, Z. L. Wang, *Adv. Mater.* **2020**, *32*, 1905696.
[15] S. Lin, X. Chen, Z. L. Wang, *Chem. Rev.* **2021**, *122*, 5209.
[16] S. Lin, L. Xu, A. Chi Wang, Z. L. Wang, *Nat. Commun.* **2020**, *11*, 399.
[17] J. Yin, X. Li, J. Yu, Z. Zhang, J. Zhou, W. Guo, *Nat. Nanotechnol.* **2014**, *9*, 378.

[18] S. S. Kwak, S. Lin, J. H. Lee, H. Ryu, T. Y. Kim, H. Zhong, H. Chen, S.-W. Kim, *ACS Nano* **2016**, *10*, 7297.
[19] A. S. Aji, R. Nishi, H. Ago, Y. Ohno, *Nano Energy* **2020**, *68*, 104370.
[20] Q. Li, Y. Zheng, D. Xiao, T. Or, R. Gao, Z. Li, M. Feng, L. Shui, G. Zhou, X. Wang, Z. Chen, *Adv. Sci.* **2020**, *7*, 2002213.
[21] F. Xing, T. Li, J. Li, H. Zhu, N. Wang, X. Cao, *Nano Energy* **2017**, *31*, 590.
[22] H. Wang, T. Yao, C. Li, L. Meng, Y. Cheng, *Chem. Eng. J.* **2020**, *397*, 125385.
[23] H. Peng, T. Liu, Y. Li, X. Wei, X. Cui, Y. Zhang, P. Xiao, *Electrochim. Acta* **2018**, *277*, 218.
[24] J. Han, T. Yan, J. Shen, L. Shi, J. Zhang, D. Zhang, *Environ. Sci. Technol.* **2019**, *53*, 12668.
[25] S. Tian, X. Zhang, Z. Zhang, *Chem. Eng. J.* **2021**, *409*, 128200.
[26] K. Zhao, W. Sun, X. Zhang, J. Meng, M. Zhong, L. Qiang, M.-J. Liu, B.-N. Gu, C.-C. Chung, M. Liu, F. Yu, Y.-L. Chueh, *Nano Energy* **2022**, *91*, 106649.
[27] E. Cha, M. D. Patel, J. Park, J. Hwang, V. Prasad, K. Cho, W. Choi, *Nat. Nanotechnol.* **2018**, *13*, 337.
[28] J. Chen, W. Tang, B. Tian, B. Liu, X. Zhao, Y. Liu, T. Ren, W. Liu, D. Geng, H. Y. Jeong, H. S. Shin, W. Zhou, K. P. Loh, *Adv. Sci.* **2016**, *3*, 1500033.
[29] Y. Guo, D. Sun, B. Ouyang, A. Raja, J. Song, T. F. Heinz, L. E. Brus, *Nano Lett.* **2015**, *15*, 5081.
[30] N. P. Kondekar, M. G. Boebinger, E. V. Woods, M. T. Mcdowell, *ACS Appl. Mater. Interfaces* **2017**, *9*, 32394.
[31] G. Gao, J. Yu, X. Yang, Y. Pang, J. Zhao, C. Pan, Q. Sun, Z. L. Wang, *Adv. Mater.* **2019**, *31*, 1806905.
[32] L. Midolo, A. Schliesser, A. Fiore, *Nat. Nanotechnol.* **2018**, *13*, 11.
[33] A. U. Rehman, M. F. Khan, M. A. Shehzad, S. Hussain, M. F. Bhopal, S. H. Lee, J. Eom, Y. Seo, J. Jung, S. H. Lee, *ACS Appl. Mater. Interfaces* **2016**, *8*, 29383.
[34] S.-L. Li, K. Komatsu, S. Nakaharai, Y.-F. Lin, M. Yamamoto, X. Duan, K. Tsukagoshi, *ACS Nano* **2014**, *8*, 12836.
[35] A. Gurarslan, S. Jiao, T.-D. Li, G. Li, Y. Yu, Y. Gao, E. Riedo, Z. Xu, L. Cao, *Adv. Mater.* **2016**, *28*, 10055.
[36] N. Sghaier, M. Prat, S. Ben Nasrallah, *Chem. Eng. J.* **2006**, *122*, 47.
[37] S. Aslan, N. Fathi Najafabadi, A. Firoozabadi, *Energy Fuels* **2016**, *30*, 2858.
[38] W. Cui, H. Ma, B. Tian, Y. Ji, F. Su, *J. Mater. Sci.* **2016**, *51*, 4031.
[39] Y. He, Q. He, L. Wang, C. Zhu, P. Golani, A. D. Handoko, X. Yu, C. Gao, M. Ding, X. Wang, F. Liu, Q. Zeng, P. Yu, S. Guo, B. I. Yakobson, L. Wang, Z. W. Seh, Z. Zhang, M. Wu, Q. J. Wang, H. Zhang, Z. Liu, *Nat. Mater.* **2019**, *18*, 1098.
[40] A. Hasani, Q. V. Le, M. Tekalgne, M.-J. Choi, T. H. Lee, H. W. Jang, S. Y. Kim, *NPG Asia Mater* **2019**, *11*, 47.
[41] T. De Silva, M. Fawzy, A. Hasani, H. Ghanbari, A. Abnavi, A. Askar, Y. Ling, M. R. Mohammadzadeh, F. Kabir, R. Ahmadi, *Nat. Commun.* **2022**, *13*, 7593.
[42] A. Valsaraj, J. Chang, A. Rai, L. F. Register, S. K. Banerjee, *2D Mater.* **2015**, *2*, 045009.
[43] M. G. Kibria, S. Zhao, F. A. Chowdhury, Q. Wang, H. P. T. Nguyen, M. L. Trudeau, H. Guo, Z. Mi, *Nat. Commun.* **2014**, *5*, 3825.
[44] Z. L. Wang, *Adv. Energy Mater.* **2020**, *10*, 2000137.
[45] N. Tessler, *J. Appl. Phys.* **2015**, *118*, 215501.
[46] R. Ahmadi, A. Abnavi, H. Ghanbari, H. Mohandes, M. R. Mohammadzadeh, T. De Silva, A. Hasani, M. Fawzy, F. Kabir, M. M. Adachi, *Nano Energy* **2022**, *98*, 107285.
[47] A. Castellanos-Gomez, J. Quereda, H. P. Van Der Meulen, N. Agraït, G. Rubio-Bollinger, *Nanotechnology* **2016**, *27*, 115705.
[48] T. Mueller, F. Xia, P. Avouris, *Nat. Photonics* **2010**, *4*, 297.
[49] A. Abnavi, R. Ahmadi, A. Hasani, M. Fawzy, M. R. Mohammadzadeh, T. De Silva, N. Yu, M. M. Adachi, *ACS Appl. Mater. Interfaces* **2021**, *13*, 45843.
[50] W. Wang, S. Gao, Y. Li, W. Yue, H. Kan, C. Zhang, Z. Lou, L. Wang, G. Shen, *Adv. Funct. Mater.* **2021**, *31*, 2101201.
[51] H. Wang, Q. Zhao, Z. Ni, Q. Li, H. Liu, Y. Yang, L. Wang, Y. Ran, Y. Guo, W. Hu, Y. Liu, *Adv. Mater.* **2018**, *30*, 1803961.
[52] K. Roy, A. Jaiswal, P. Panda, *Nature* **2019**, *575*, 607.
[53] J. Yu, X. Yang, G. Gao, Y. Xiong, Y. Wang, J. Han, Y. Chen, H. Zhang, Q. Sun, Z. L. Wang, *Sci. Adv.* **2021**, *7*, eabd9117.
[54] X. Yang, J. Yu, J. Zhao, Y. Chen, G. Gao, Y. Wang, Q. Sun, Z. L. Wang, *Adv. Funct. Mater.* **2020**, *30*, 2002506.
[55] M. Jia, P. Guo, W. Wang, A. Yu, Y. Zhang, Z. L. Wang, J. Zhai, *Sci. Bull.* **2022**, *67*, 803.
[56] F. Zhang, C. Li, Z. Li, L. Dong, J. Zhao, *Microsyst. Nanoeng.* **2023**, *9*, 16.
[57] S. Z. Bisri, S. Shimizu, M. Nakano, Y. Iwasa, *Adv. Mater.* **2017**, *29*, 1607054.
[58] H. Wan, Y. Gan, J. Sun, T. Liang, S. Zhou, P. Wang, *Sens. Actuators, B* **2019**, *299*, 126952.
[59] J. Li, N. S. Ha, T. '.L.'. Liu, R. M. Van Dam, C.-J. 'Cj' Kim, *Nature* **2019**, *572*, 507.
[60] P. Robin, T. Emmerich, A. Ismail, A. Niguès, Y. You, G.-H. Nam, A. Keerthi, A. Siria, A. K. Geim, B. Radha, L. Bocquet, *Science* **2023**, *379*, 161.
[61] Y. Wan, E. Li, Z. Yu, J.-K. Huang, M.-Y. Li, A.-S. Chou, Y.-T. Lee, C.-J. Lee, H.-C. Hsu, Q. Zhan, A. Aljarb, J.-H. Fu, S.-P. Chiu, X. Wang, J.-J. Lin, Y.-P. Chiu, W.-H. Chang, H. Wang, Y. Shi, N. Lin, Y. Cheng, V. Tung, L.-J. Li, *Nat. Commun.* **2022**, *13*, 4149.
[62] Y. Gao, Z. Liu, D.-M. Sun, L. Huang, L.-P. Ma, L.-C. Yin, T. Ma, Z. Zhang, X.-L. Ma, L.-M. Peng, H.-M. Cheng, W. Ren, *Nat. Commun.* **2015**, *6*, 8569.
[63] C. Cong, J. Shang, Y. Wang, T. Yu, *Adv. Opt. Mater.* **2018**, *6*, 1700767.
[64] T. A. J. Loh, D. H. C. Chua, A. T. S. Wee, *Sci. Rep.* **2015**, *5*, 18116.
[65] A. Hasani, Q. Van Le, M. Tekalgne, M.-J. Choi, S. Choi, T. H. Lee, H. Kim, S. H. Ahn, H. W. Jang, S. Y. Kim, *ACS Appl. Mater. Interfaces* **2019**, *11*, 29910.
[66] G. Quincke, *Ann. Phys.* **1861**, *189*, 513.
[67] P. Yang, X. Qu, K. Liu, J. Duan, J. Li, Q. Chen, G. Xue, W. Xie, Z. Xu, J. Zhou, *ACS Appl. Mater. Interfaces* **2018**, *10*, 8010.
[68] R. Zhang, S. Wang, M.-H. Yeh, C. Pan, L. Lin, R. Yu, Y. Zhang, L. Zheng, Z. Jiao, Z. L. Wang, *Adv. Mater.* **2015**, *27*, 6482.
[69] B. Bourlon, J. Wong, C. Mikó, L. Forró, M. Bockrath, *Nat. Nanotechnol.* **2007**, *2*, 104.
[70] J. C. Farmer, D. V. Fix, G. V. Mack, R. W. Pekala, J. F. Poco, *J. Electrochem. Soc.* **1996**, *143*, 159.
[71] A. Fujishima, K. Honda, *Nature* **1972**, *238*, 37.
[72] P. Bergveld, *IEEE Trans. Biomed. Eng.* **1970**, *BME-17*, 70.
[73] Z.-H. Lin, G. Cheng, L. Lin, S. Lee, Z. L. Wang, *Angew. Chem., Int. Ed.* **2013**, *52*, 12545.